

Crystal Structure and Magnetic Properties of (Fe,Si,Al)-Based Nanocomposite Magnets Designed for Cryogenic Applications



MARIA DANIIL, HELEN M. FONDA, and MATTHEW A. WILLARD

In this work, we performed a detailed study of the crystallization, crystal structure, and magnetic properties of $\text{Fe}_{87-z}\text{Si}_{z-x}\text{Al}_x\text{Nb}_3\text{B}_9\text{Cu}_1$ nanocrystalline alloys that were designed primarily for low-temperature applications. In addition, their interesting low-temperature [77 K to 300 K (-196°C to 27°C)] magnetic properties (H_c and M_s) were also investigated. These alloys were produced by annealing their amorphous precursors at 823 K (550°C). Si and Al substitution do not seem to alter the crystallization procedure and crystal structure of the parent alloy but reduces the lattice parameter, the Curie temperature, and the saturation magnetization. On the other hand, it improves the room temperature coercivity at small amounts ($H_c = 0.35$ A/m for $x = 3.5$, $z = 19$) and changes its temperature dependence. As a result, a remarkably low H_c value at 77 K (-196°C) of 0.45 A/m was observed for $x = 6$ and $z = 23.5$.

DOI: 10.1007/s40553-015-0051-z

© ASM International (ASM) and The Minerals, Metals & Materials Society (TMS) 2015

I. INTRODUCTION

FOR decades, Finemet [*e.g.*, $\text{Fe}_{73.5}\text{Si}_{13.5}\text{Nb}_3\text{B}_9\text{Cu}_1$] has been a leading material for soft magnet applications at room temperature.^[1] Its excellent soft magnetic properties have been attributed to the very fine microstructure that results in nearly zero effective magnetocrystalline anisotropy^[2,3] and very small magnetostriction.^[4] Due to its successful room temperature performance, a recent study by Claassen^[5] investigated Finemet for use in cryogenic environments to support superconducting motor and cryogenic power converter technologies. The study revealed that the core losses of Finemet increase by nearly 300 pct compared to its room temperature value. Other materials designed for room temperature use have also been investigated for cryogenic applications, exhibiting varying degrees of degraded performance.^[5-9] With all of the materials investigated showing some performance degradation due to the cryogenic environment, it is clear that there is room for new alloys specifically designed for cryogenic temperatures if ferromagnetic materials are going to be considered for use within the cryostat.

Previous work by our group showed that proper substitutions of Fe with Al and Si in the (Fe,Si)-based nanocrystalline alloys can improve the magnetic properties both at ambient and liquid nitrogen environments.^[10] In the present work, we investigate the crystallization behavior, crystal structure, Curie tem-

perature, magnetostriction, and temperature dependence of saturation magnetization and coercivity of Fe-Si-Al-Nb-Cu alloys. The alloy design principles for the Al/Si substitution were inspired by the work of Takahashi *et al.* on single crystalline and polycrystalline Sendust alloy (7 to 11 wt pct Si, 4 to 7 wt pct Al, bal. Fe).^[11,12] In their work, the temperature dependence of magnetocrystalline anisotropy (K_1) and magnetostriction coefficients (λ_{100} , λ_{111}) for Fe-Si-Al compositions close to the Sendust alloy were examined. They found the temperature at which K_1 and λ_s near zero depends sensitively on the Fe-Si-Al composition. The minimum temperature at which these two criteria were satisfied was 195 K (or -78°C). In the present study, we have used a linear extrapolation of the Takahashi data to identify a composition region with potentially low values of K_1 and λ_s at 77 K (-196°C).

II. EXPERIMENTAL PROCEDURE

Amorphous ribbons with composition $\text{Fe}_{87-z}\text{Si}_{z-x}\text{Al}_x\text{Nb}_3\text{B}_9\text{Cu}_1$ where $(x, z) = (0, 13.5), (3.5, 19), (5, 21.5), (6, 23.5), (7, 25)$ were prepared using a single roller melt spinner with a surface speed of 50 m/s and an orifice of 0.75 mm in a He environment. The ribbons produced had a thickness of ~ 20 μm , width of 2 to 3 mm, and lengths between a few centimeters and several meters. The as-spun ribbons were annealed isothermally at 823 K and 1023 K (550°C and 750°C) for 3600 seconds in an Argon atmosphere and then quenched rapidly in water. The crystallization process was examined by differential thermal analysis (DTA) using a TA instruments SDT2960 at a heating rate of 20 K (-253°C)/min. The crystal structure of the as-spun and annealed ribbons was examined using a Philips APD 3520 X-ray diffractometer (XRD). The

MARIA DANIIL, Researcher, and MATTHEW A. WILLARD, Associate Professor, are with the Department of Materials Science and Engineering, Case Western Reserve University, Cleveland, OH 44106. Contact e-mail: maw169@case.edu HELEN M. FONDA, Research Analyst, formerly with the Physics Department, Johns Hopkins University, Baltimore, MD 21218, is now with the Department of Justice, Washington, DC.

Manuscript submitted March 25, 2015.

Article published online May 19, 2015

measurements were performed on ~1-cm-long pieces of ribbons using Cu K_α radiation. From the XRD patterns, we calculated the lattice constants of the crystalline phase (by fitting the diffraction peaks and using the $\cos^2\theta/\sin\theta$ method) and the grain size (using the Scherrer equation).^[13] The magnetic hysteresis loops and thermomagnetic measurements were measured using an ADE Model 4HF vibrating sample magnetometer (VSM). During these measurements, a piece of ribbon 5-7-mm long was mounted with its long dimension parallel to the external field in order to minimize the demagnetizing field effect. The hysteresis loops of the samples annealed at 823 K (550 °C) were measured at temperatures between 77 K and 300 K (−196 °C and 27 °C) and with applied fields up to 1.592 MA/m (20 kOe). For the determination of the coercivity, each ribbon piece was measured 5 to 10 times and an average value was obtained. Thermomagnetic measurements were conducted under an applied field of 3.18 kA/m (40 Oe) from 25 to 350 °C. Transmission electron microscopy (TEM) was carried out to examine the refined grain microstructure using a Philips CM-30 analytical transmission electron microscope. Samples for TEM were prepared by ion milling using a Fischione ion mill with a gun voltage of 5 kV, current of 5 mA,

and sputtering angle of 12 deg. Magnetostriction measurements were performed using strain gage-based techniques described in Reference 14.

III. RESULTS AND DISCUSSION

Figure 1 shows the DTA scans of the as-spun ribbons with the values of the onset of the crystallization temperatures presented in Table I. All compositions show two strong exothermic peaks that are well separated from each other. The first one occurs between 810 K and 829 K (537 °C and 556 °C) and the second between 961 K and 1003 K (688 °C and 730 °C). Some compositions show a weak third exothermic peak between 1008 K and 1040 K (735 °C and 767 °C). It can be seen from Figure 1 that the position of the first exothermic peak varies only slightly with Al and Si additions when compared to that of Finemet. However, the second peak moves to higher temperatures when x increases from 0 to 3.5 followed by small fluctuations for higher x values. Overall, the difference between the primary and the secondary crystallization peak positions increases significantly with 3.5 at. pct substitution of Al followed by small decrease for 6 and 7 at. pct Al (Table I). These results imply that Si and Al substitutions improve the stability of the intergranular amorphous matrix phase that forms during primary crystallization compared to the Finemet composition (*i.e.*, $\text{Fe}_{73.5}\text{Si}_{13.5}\text{Nb}_3\text{B}_9\text{Cu}_1$). The first exothermic peak, according to X-ray diffractometry, corresponds to the crystallization of the as-spun, amorphous phase to the $\text{Fe}_3(\text{Si},\text{Al})$ phase (see also Figure 2), while the second crystallization peak is likely due to the clear formation of Fe_3B , Fe_2B phases and possibly Fe-Nb intermetallics from the residual amorphous matrix phase that persists after primary crystallization.

Figure 2 shows the XRD patterns of $\text{Fe}_{65.5}\text{Si}_{16.5}\text{Al}_5\text{Nb}_3\text{B}_9\text{Cu}_1$ ribbons before and after annealing. Similar diffractograms were obtained for all compositions. The ribbons in the as-spun state are clearly amorphous (Figure 2(a)). After annealing at 823 K (550 °C) for 3600 seconds (which is approximately the temperature where the primary crystallization peak occurs), the $\text{D0}_3\text{-Fe}_3(\text{Si},\text{Al})$ phase is formed as identified from the broad fundamental peaks and many weak superlattice peaks, especially $\{111\}$ and $\{200\}$. In addition to the crystalline phase, some residual amorphous phase exists as indicated from the extra breadth of the $\{220\}$ fundamental peak (Figure 2(b)). The fact that the $\text{D0}_3\text{-Fe}_3(\text{Si},\text{Al})$ is formed in such a wide range of Fe-Si-Al compositions is due to the large solubility of Si and

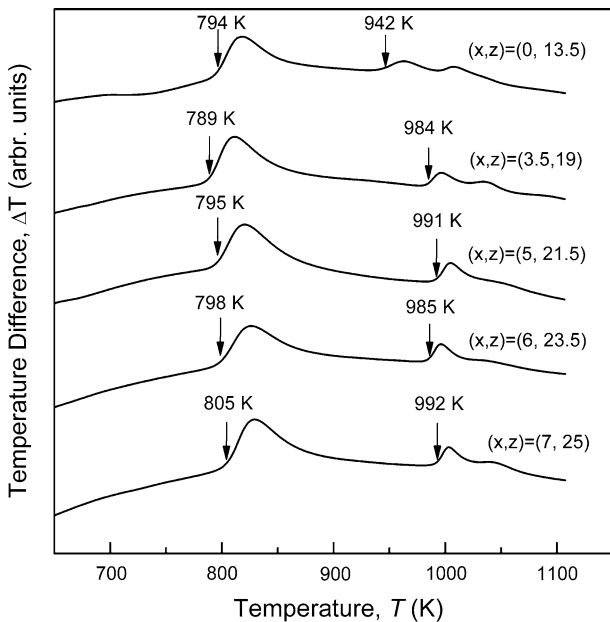


Fig. 1—Differential Thermal Analysis scans of the amorphous as-spun ribbons at a heating rate of 20 K (−253 °C)/min for $\text{Fe}_{87-x}\text{Si}_{17.5-x}\text{Al}_x\text{Nb}_3\text{B}_9\text{Cu}_1$ alloys.

Table I. Thermal Analysis for the as-spun $\text{Fe}_{87-x}\text{Si}_{17.5-x}\text{Al}_x\text{Nb}_3\text{B}_9\text{Cu}_1$ Ribbons

Composition	$T_{x1,\text{onset}}$ [K (°C)]	$T_{x2,\text{onset}}$ [K (°C)]	ΔT_x [K (°C)]
$\text{Fe}_{73.5}\text{Si}_{13.5}\text{Nb}_3\text{B}_9\text{Cu}_1$	794 (521)	942 (669)	148 (−125)
$\text{Fe}_{68}\text{Si}_{15.5}\text{Al}_{3.5}\text{Nb}_3\text{B}_9\text{Cu}_1$	789 (516)	984 (711)	195 (−78)
$\text{Fe}_{65.5}\text{Si}_{16.5}\text{Al}_5\text{Nb}_3\text{B}_9\text{Cu}_1$	795 (522)	991 (718)	196 (−77)
$\text{Fe}_{63.5}\text{Si}_{17.5}\text{Al}_6\text{Nb}_3\text{B}_9\text{Cu}_1$	798 (525)	985 (712)	187 (−86)
$\text{Fe}_{62}\text{Si}_{18}\text{Al}_7\text{Nb}_3\text{B}_9\text{Cu}_1$	805 (532)	992 (719)	187 (−86)

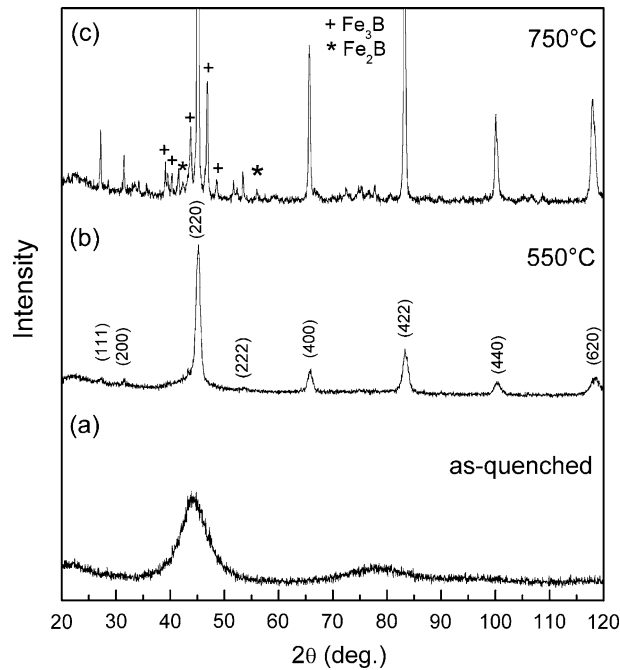


Fig. 2—X-ray Diffraction patterns of $\text{Fe}_{63.5}\text{Si}_{17.5}\text{Al}_6\text{Nb}_4\text{B}_9\text{Cu}_1$ ribbons: (a) as-spun, (b) annealed at 823 K (550 °C)/3600 s ((*hkl*) shown for D_{03} phase), and (c) annealed at 1023 K/3600 s (additional peaks marked for Fe_3B (+) and Fe_2B (*) phases).

Al in the D_{03} phase. After annealing at 750 °C (Figure 2(c)) (which corresponds to a temperature well above the second crystallization peak), some additional intermetallic phases form (namely Fe_2B and Fe_3B). The Fe-B compounds have tetragonal structure with stronger magnetocrystalline anisotropy^[8,15] which in combination with the coarsening of the grains (narrower diffraction peaks) contributes to the deterioration the soft magnetic properties of the alloy. Based on the breadth of the XRD peaks and using the Scherrer formula, we found that the average grain size for the samples annealed at 823 K (550 °C) is between 9 and 11 nm diameter, independent of composition. This was confirmed by the TEM results as shown in the bright-field image of the $\text{Fe}_{63.5}\text{Si}_{17.5}\text{Al}_6\text{Nb}_3\text{B}_9\text{Cu}_1$ ribbons annealed at 823 K (550 °C) (Figure 3). It can be clearly seen that the ribbon is composed of very small grains 10 to 15 nm in diameter embedded in an amorphous matrix. The selected area diffraction (SAD) shown in the inset of Figure 3 confirms the crystal structure of the $\text{Fe}_3(\text{Si,Al})$ grains.

From the XRD peaks, we calculated the lattice constant of the D_{03} structure and the results are plotted as a function of z (*i.e.* total Si + Al substitution for Fe) in Figure 4. It can be seen that the lattice constant decreases as z increases. This means that when Fe is replaced by Si and Al atoms, the D_{03} unit cell becomes smaller. Due to the smaller size of the Al and Si, the non-equilibrium nature of the processing, and the changes in the complex nature of lattice parameter with the composition in Fe-Si-Al alloys, a unique composition of the D_{03} phase was not determined. Previous studies on Fe-Si alloys showed a linear decrease in the lattice parameter with the Si content.^[16] However, Fe-Al

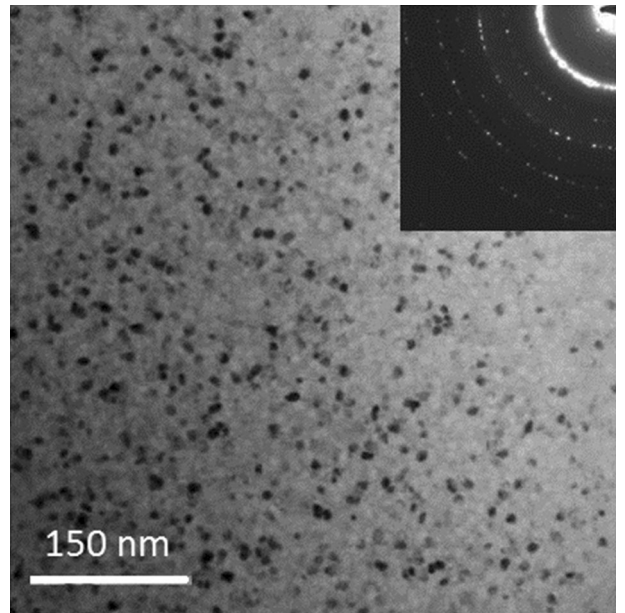


Fig. 3—Bright-field TEM image of $\text{Fe}_{63.5}\text{Si}_{17.5}\text{Al}_6\text{Nb}_4\text{B}_9\text{Cu}_1$ annealed at 823 K (550 °C)/3600 s. The inset on the top right corner is a selected area diffraction image showing the diffraction rings from the D_{03} nanocrystals.

alloys showed a more complicated trend which is closely related to the changes in the magnetic valence with the Al content.^[17] In particular, they found that the lattice parameter in Fe-Al alloys increases up to ~22 at. pct Al, then it decreases up to ~33 at. pct Al. According to Taylor and Jones,^[17] this complexity can be attributed to the electron transfer to the Fe sites as Al is substituted for Fe, thus decreasing both the radii of Fe and Al. Another reason for the observed trend in our alloys is the fact that a significant portion of the Al atoms does not enter the D_{03} structure but is segregated in the Cu clusters in a ratio 2:1 as suggested by the previous 3D atom probe analysis^[18] making the effect of Si on the crystal lattice parameter dominant.

Since in these alloys the averaging of the magnetocrystalline anisotropy is facilitated through the ferromagnetic intergranular amorphous phase, it is important to know the Curie temperature of the amorphous phase (T_c^{am}), which dictates the upper temperature limit for applications. The Curie temperature of the as-quenched amorphous and the $\text{Fe}_3(\text{Si,Al})$ phases in the annealed samples at 823 K (550 °C) vs z is shown in Figure 5 and delineated in Table II. Two trends can be discerned: (1) the Curie temperature of the $\text{Fe}_3(\text{Si,Al})$ phase is generally higher than that of the amorphous phase; (2) the Curie temperature of each phase decreases with Al + Si substitution.^[18] As suggested by the previously published atom probe tomography analysis, B and Nb atoms are strongly segregated in the residual amorphous phase whereas Fe, Si, and some of the Al atoms in the nanocrystalline phase. Therefore, the Fe substitution with Si and Al is expected to have a stronger effect on the crystalline than the amorphous phase. In addition, this declining trend of the Curie temperatures can be

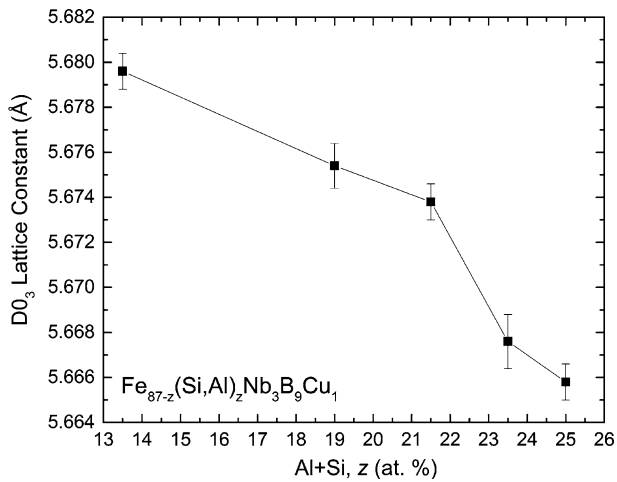


Fig. 4—Effect of Si and Al substitution for Fe on the lattice constant of the D0₃-Fe₃(Si,Al) grains for the Fe_{87-z}Si_{z-x}Al_xNb₃B₉Cu₁ alloys annealed at 823 K (550 °C)/3600 s.

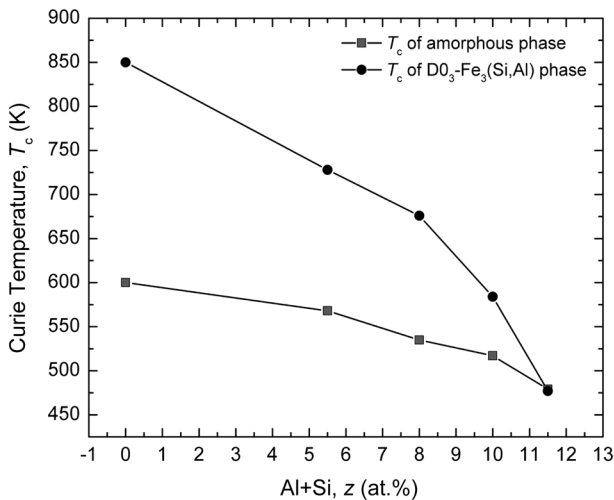


Fig. 5—Curie temperature of the amorphous phase in the as-spun ribbons and the crystalline phase in the annealed ribbons [at 823 K (550 °C)/3600 s] with compositions Fe_{87-z}Si_{z-x}Al_xNb₃B₉Cu₁.

attributed to the weakening of the ferromagnetic interactions due to the Si and Al substitutions. Similar trends have been observed in the Fe-Si-Al ordered alloys^[19] and Fe-Si-B alloys.^[20]

The effect of composition and annealing on the room temperature saturation magnetization of the as-spun and annealed ribbons is illustrated in Figure 6 with the room temperature saturation magnetization values presented in Table II. In both the as-spun and annealed ribbons, the magnetization decreases monotonically with the amount of Si + Al substitution for Fe, z . The decrease becomes steeper for the last two compositions, $z = 23.5, 25$. This trend can be attributed to (1) the absence of d-electrons in Si and Al atoms that dilute the magnetic moment of the alloy as they substitute for Fe in the parent composition (Finemet), (2) the electron transfer from Si and Al to Fe atoms reducing the Fe atomic moment,^[17] and (3) the fast decrease of the Curie

temperature of both the as-spun amorphous phase and the crystalline D0₃-Fe₃(Si,Al) phase with z as discussed earlier. Another observation from Figure 6 is that after annealing, the saturation magnetization of the ribbons decreases slightly for the Finemet composition ($z = 13.5$) up to 35 pct in the Fe₆₂Si₁₈Al₇Nb₃B₉Cu₁ ($z = 25$) ribbons.

The room temperature coercivity, H_c , (Figure 7(a)) shows a minimum of 0.35 A/m for $z = 19$. Then it increases steadily with the increasing z , reaching 1.48 A/m for $z = 25$.^[10] All the room temperature coercivity values are summarized in Table II. Similar coercivity trends in Al-containing Finemet compositions have been observed by Todd *et al.*^[21] In nanocrystalline materials, the coercivity is a result of the average magnetocrystalline anisotropy, $\langle K \rangle$, rather the magnetocrystalline anisotropy constant, K_1 , due to the small grain size and the exchange interaction between them.^[3] Room temperature $\langle K \rangle$ values were calculated using the H_c and M_s values from our measurements and Herzer's equations for H_c and $\langle K \rangle$ in the following way. First, we used the $\langle K \rangle = K_1^4 \cdot D^6 / J_s \cdot A^3$ (where $D =$ grain size, $A \approx 10^{-11}$ J/m = exchange stiffness, $J_s =$ saturation magnetization in Tesla, and K_1 (Fe-20 at. pct Si) = 8×10^3 J/m) equation^[3] to calculate $\langle K \rangle$ for the Finemet composition ($x = 0, z = 13.5$). By plugging this value into $H_c = p_c \cdot \langle K \rangle / J_s$ (where p_c is a constant and J_s the magnetization in Tesla), we found that $p_c = 0.138$. Assuming that p_c does not change over the composition range, we used the relation $\langle K \rangle = H_c \cdot J_s / p_c$ to find the $\langle K \rangle$ for the rest of the compositions. The results are shown in Figure 7(b) where it can be seen that $\langle K \rangle$ follows the same trend as the coercivity.

Since the coercivity in the soft nanocrystalline alloys not only depends on the average magnetocrystalline anisotropy $\langle K \rangle$,^[2] but also on the magnetostriction, the room temperature magnetostrictive coefficient, λ_s , was also measured across the composition series. The results of the as-spun and annealed samples are shown in Figure 8. The magnetostriction coefficient in the as-spun ribbons has large positive values due to the presence of the amorphous phase and it declines with the increasing Al + Si substitution. After annealing at 823 K (550 °C), their magnetostriction values drop close to zero and for higher Al and Si amounts become slightly negative. This is a result of two contributions of opposite sign, a positive one from the amorphous phase and a negative one from the Fe-Si-Al crystallites.^[3] Similar behavior has been observed in other Finemet compositions with and without Al.^[4,22,23] From the measured λ_s values and assuming that the residual stress in the ribbons is $\sigma \approx 1.5$ MPa^[8] and independent of the composition, the stress anisotropy constant was calculated based on $K_\sigma = 3/2 \cdot \lambda_s \cdot \sigma$. The results are shown in Figure 7(b) where it can be seen that for all the Al-containing compositions, K_σ is an order of magnitude or two smaller than the $\langle K \rangle$ values. Therefore, we can safely assume that the main contribution of the coercivity at room temperature is the average magnetocrystalline anisotropy, $\langle K \rangle$.

Since these alloys were primarily designed to have optimum magnetic properties at cryogenic tem-

Table II. Magnetic parameters at 300 K and 77 K (27 °C and −196 °C) of the $\text{Fe}_{87-z}\text{Si}_{z-x}\text{Al}_x\text{Nb}_3\text{B}_9\text{Cu}_1$ ribbons annealed at 823 K (550 °C) for 3600 s

Composition	M_S (300 K) A m ² /kg	M_S (77 K) A m ² /kg	H_c (300 K) A/m	H_c (77 K) A/m	T_c (am) (K)	T_c ($\text{Fe}_3(\text{Si},\text{Al})$) (K)
$\text{Fe}_{73.5}\text{Si}_{13.5}\text{Nb}_3\text{B}_9\text{Cu}_1$	145	158.4	0.52 ± 0.08	0.81	600 (327)	850 (577)
$\text{Fe}_{68}\text{Si}_{15.5}\text{Al}_{3.5}\text{Nb}_3\text{B}_9\text{Cu}_1$	113.3	127.6	0.35 ± 0.05	1.26	568 (295)	728 (455)
$\text{Fe}_{65.5}\text{Si}_{16.5}\text{Al}_5\text{Nb}_3\text{B}_9\text{Cu}_1$	98.3	114.9	0.50 ± 0.07	0.58	535 (262)	676 (403)
$\text{Fe}_{63.5}\text{Si}_{17.5}\text{Al}_6\text{Nb}_3\text{B}_9\text{Cu}_1$	80.4	99.3	1.12 ± 0.18	0.45	517 (244)	584 (311)
$\text{Fe}_{62}\text{Si}_{18}\text{Al}_7\text{Nb}_3\text{B}_9\text{Cu}_1$	64.1	87.9	1.48 ± 0.15	1.45	479 (206)	476 (203)

$T_c(\text{am})$ = Curie temperature of the as-quenched amorphous phase and $T_c(\text{Fe}_3(\text{Si},\text{Al}))$ = Curie temperature of D0_3 crystalline phase.

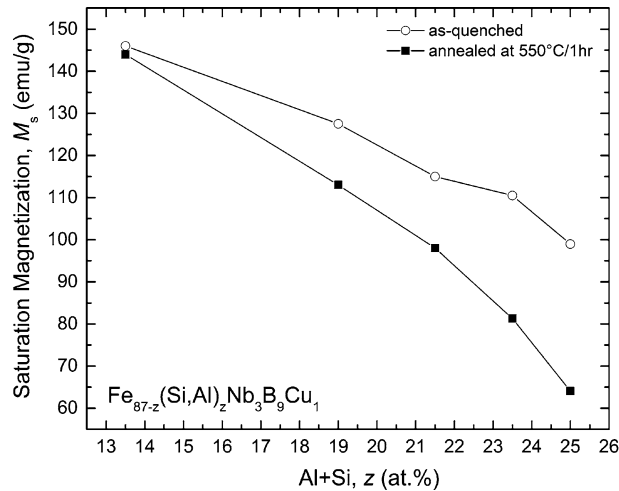


Fig. 6—Variation of the room temperature saturation magnetization with composition for the as-spun and annealed [at 823 K (550 °C)/3600 s] $\text{Fe}_{87-z}\text{Si}_{z-x}\text{Al}_x\text{Nb}_3\text{B}_9\text{Cu}_1$ alloys.

peratures, it is important to investigate their magnetic performance not only at room temperature but also at lower temperatures. The results are summarized in Figure 9 where the temperature dependence of the saturation magnetization (M_S) and coercivity (H_c) of the annealed ribbons are plotted. As expected, M_S increases steadily as the measuring temperature decreases due to the reduced thermofluctuations of the magnetic moments. The increase seems to be slightly stronger for the ribbons with the highest amount of Al and Si contents (Figure 9(a)). This is probably due to the lower Curie temperatures associated with these compositions. On the other hand, the temperature dependence of the coercivity is more complicated and changes significantly with the addition of Al and Si (z) (Figure 9(b)).

For the first three compositions ($z = 13.5, 19,$ and 21.5), coercivity increases as temperature decreases. More specifically for $z = 13.5$ and 21.5 , H_c reaches a shallow maximum at $T = 200$ K (-73 °C) before it begins to slightly decline at lower temperatures, whereas for $z = 19$ it increases continuously. At $z = 23.5$ and 25 , the temperature trend of the coercivity reverses; H_c decreases with the decrease in temperature to about 150 K (-123 °C) and then either remains stable ($z = 23.5$) or increases slightly ($z = 25$). The lowest measured coercivity at 77 K (-196 °C) is 0.45 A/m and it was obtained for $z = 23.5$. This value is lower than

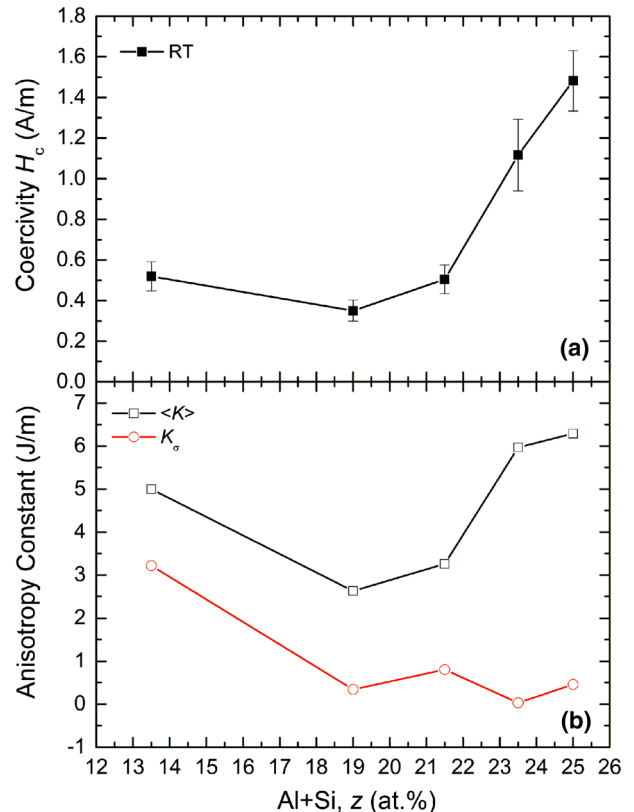


Fig. 7—Room temperature coercivity of the annealed ribbons for varying $\text{Fe}_{87-z}\text{Si}_{z-x}\text{Al}_x\text{Nb}_3\text{B}_9\text{Cu}_1$ compositions (a) and calculated average magnetocrystalline anisotropy (K) and stress anisotropy, K_σ constants (b).

that of the commercially available Cryoperm-10 alloy (*i.e.*, $\text{Ni}_{77.4}\text{Fe}_{15.9}\text{Cu}_{4.2}\text{Mo}_{1.5}\text{Mn}_{1.0}$) designed by Vacuum-schmelze to operate at 4.2 to 77 K (-196 °C), which has an H_c of 1.2 A/m.^[10]

The different temperature trends of the coercivity we observed can be attributed to the combined effect of temperature dependence of the magnetocrystalline anisotropy and magnetostriction. By changing the ratio of Fe:Si:Al, we change the temperature where both K_1 and λ have values near zero, which enable lower coercivity. A rarely observed change in the sign of K_1 requires a zero value at some temperature, which is sensitively dependent on the composition of the alloy. This specific feature of (Fe,Si,Al) alloys was observed by Takahashi, *et al.* using FeSiAl single-crystal samples and

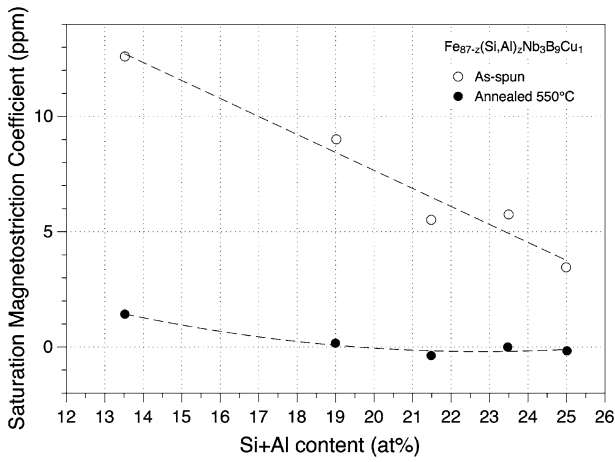


Fig. 8—Room temperature saturation magnetostriction as a function of composition for the as-spun and annealed [at 823 K (550 °C) 3600 s] $\text{Fe}_{87-z}\text{Si}_{z-x}\text{Al}_x\text{Nb}_3\text{B}_9\text{Cu}_1$ alloys.

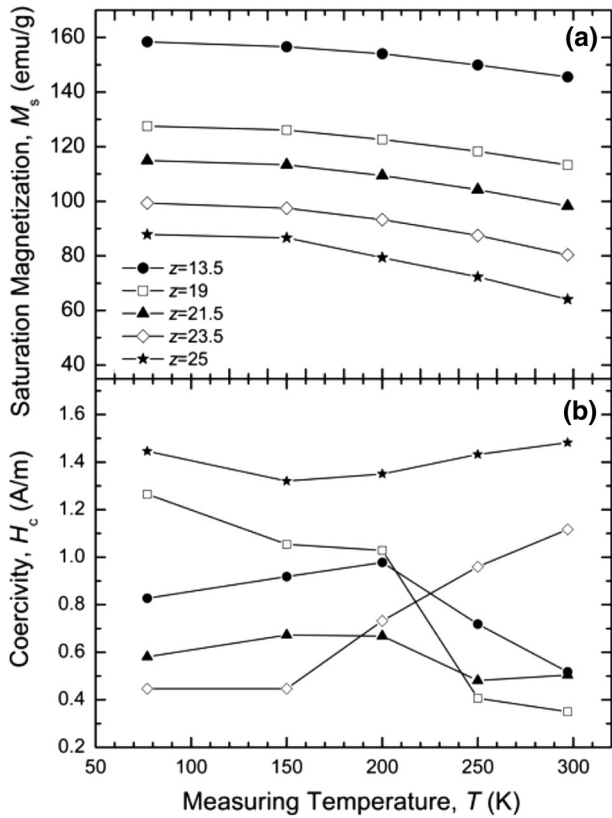


Fig. 9—Low temperature dependence of (a) the saturation magnetization (M_s) and (b) coercivity (H_c) of the annealed [823 K (550 °C)/3600 s] $\text{Fe}_{87-z}\text{Si}_{2-x}\text{Al}_x\text{Nb}_3\text{B}_9\text{Cu}_1$ ribbons.

is illustrated in Figure 3 of Reference 12 and Figure 2 in Reference 11. This known change in sign with composition in ‘large-grained’ (or single crystal) alloys was used as an alloy design principle for the development of fine-grained alloys. Although we did not measure the temperature dependence of the magnetocrystalline anisotropy in our samples, we believe that like in Takahashi alloys the slight variation in Si/Al content for

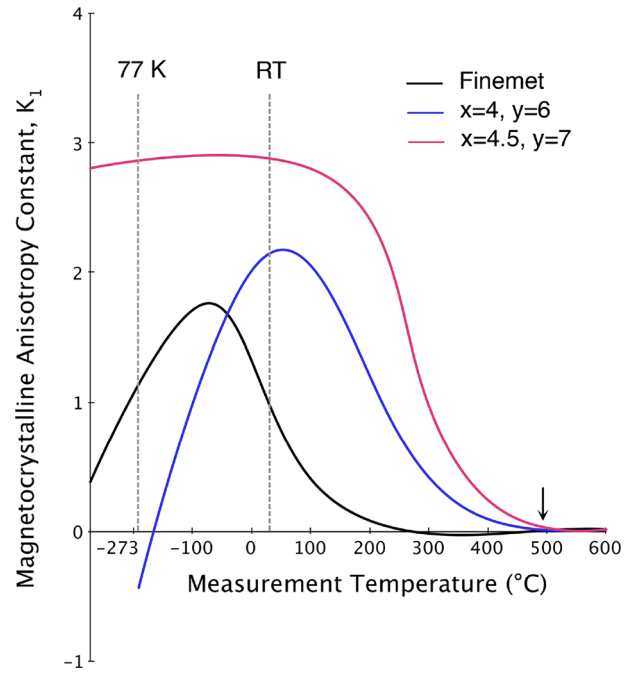


Fig. 10—Schematic diagram of the proposed variation in magnetocrystalline anisotropy for three of the $\text{Fe}_{87-z}\text{Si}_{2-x}\text{Al}_x\text{Nb}_3\text{B}_9\text{Cu}_1$ alloys ($z = 13.5, 23.5, \text{ and } 25$).

the related alloys results in a large change in the temperature at which the magnetocrystalline anisotropy changes sign. A schematic diagram that is consistent with what we know about the $K_1(T)$ for (Fe,Si,Al), (Fe,Si), and our samples is graphically shown in Figure 10 for three representative compositions. Of course, the temperature dependence of magnetostriction is another factor that determines the coercivity at low temperatures too; however, we were also unable to measure this quantity at cryogenic temperatures. In addition, as it was mentioned earlier, the magnetostriction in these nanocomposite ribbons has two contributions of opposite sign, i.e., from the Fe-Si-Al grains and the amorphous matrix, which may have completely different temperature trends. According to Takahashi^[11] in the Fe-Si-Al single crystals, both magnetostrictive coefficients, λ_{100} and λ_{111} , change sign from negative to positive with the decreasing temperature. However, it is not known how the magnetostrictive coefficient of the amorphous phase varies with temperature making it even more difficult to predict the non-equilibrium multiphase samples.

IV. CONCLUSIONS

In this work, we successfully designed and fabricated a series of (Fe-Si-Al)-based soft nanocrystalline alloys with the intention of improving their magnetic performance at cryogenic temperatures. It was found that Si and Al substitutions for Fe has the following effects:

1. Stabilize the nanocrystalline $\text{D0}_3\text{-Fe}_3(\text{Si,Al})$ microstructure by increasing the temperature differ-

ence between the primary and secondary crystallization peak.

2. Decrease the lattice parameter of the $D0_3$ - $Fe_3(Si,Al)$ phase, the Curie temperature of the amorphous and the crystalline phase, and the saturation magnetization of the ribbons.
3. Decrease the room temperature coercivity to 0.35 A/m when used at small amounts ($x = 3.5$, $z = 19$).
4. Change the temperature dependence of the coercivity. The lowest coercivity, 0.45 A/m, was obtained at 77 K (-196 °C) for the $Fe_{63.5}Si_{17.5}Al_6Nb_3B_9Cu_1$ ribbons, which is comparatively lower than that obtained for the commercially available alloy, and hence is favorable for cryogenic applications.

ACKNOWLEDGMENTS

The authors would like to acknowledge the help of R. Goswami in the measurement of TEM samples. The work was supported by the Office of Naval Research under contract N00014-12-WX-2-1328. This work was completed in part at the U.S. Naval Research Laboratory.

REFERENCES

1. Y. Yoshizawa, S. Oguma, and K.Y. Yamaguchi: *J. Appl. Phys.*, 1988, vol. 64 (10), pp. 6044–46.
2. G. Herzer: *IEEE Trans. Magn.*, 1989, vol. MAG-25 (5), pp. 3327–29.
3. G. Herzer: *Mater. Sci. Eng. A*, 1991, vol. 133, pp. 1–5.

4. V.H. Duong, R. Grössinger, R. Sato Turtelli, and Ch. Pola: *J. Magn. Magn. Mater.*, 1996, vols. 157–158, pp. 193–94.
5. J.H. Claassen: *IEEE Trans. Appl. Supercond.*, 2005, vol. 15 (2), pp. 2385–88.
6. T. Nakata, N. Takahashi, K. Fugiwara, M. Nagano, and M. Seno: *J. Magn. Magn. Mater.*, 1992, vol. 112, pp. 174–76.
7. M. Chen, Y.J. Yu, L.Y. Xiao, Q.L. Wang, W. Chung, K. Lim, and S.K. Baang: *IEEE Trans. Appl. Supercond.*, 2003, vol. 13, pp. 2313–16.
8. M.A. Willard and M. Daniil: *Handbook of Magnetic Materials, Chap. 4*, Elsevier, Amsterdam, 2013, vol. 21, pp. 173–342.
9. M.A. Willard and T.M. Heil: *J. Appl. Phys.*, 2007, vol. 101, p. 09N113.
10. M. Daniil, M.S. Osofsky, D.U. Gubser, and M.A. Willard: *Appl. Phys. Lett.*, 2010, vol. 96, p. 162504.
11. M. Takahashi, H. Arai, and T. Wakiyama: *IEEE Trans. Magn.*, 1987, vol. MAG-23 (5), pp. 3523–25.
12. M. Takahashi, H. Arai, Y. Tanaka, and T. Wakiyama: *IEEE Trans. Magn.*, 1986, vol. MAG-22, pp. 638–40.
13. B.D. Cullity: *Elements of X-Ray Diffraction*, 2nd ed., Addison-Wesley, Reading, MA, 1978, pp. 102, 359–63.
14. J.H. Claassen, M.A. Willard, and V.G. Harris: *Rev. Sci. Instr.*, 2002, vol. 73 (9), pp. 3265–67.
15. R. Coehoorn, D.B. de Mooij, and C. de Waard: *J. Magn. Magn. Mater.*, 1989, vol. 80, pp. 101–04.
16. L.K. Varga, F. Mazaleyrat, J. Kovac, and J.M. Greneche: *J. Phys. Condens. Mater.*, 2002, vol. 14, pp. 1985–2000.
17. A. Taylor and R.M. Jones: *J. Phys. Chem. Solids*, 1958, vol. 6, pp. 16–37.
18. M. Daniil, K.E. Knipling, H.M. Fonda, and M.A. Willard: *New J. Phys.*, 2014, vol. 16, p. 055016.
19. E. Legarra, E. Apiñaniz, F. Plazaola, J.A. Jimenez, and A.R. Pierna: *J. Magn. Magn. Mater.*, 2008, vol. 320, pp. e688–91.
20. F.E. Luborsky, J. Becker, J. Walter, and H. Liebermann: *IEEE Trans. Magn.*, 1979, vol. 15 (3), pp. 1146–49.
21. I. Todd, B.J. Tate, H.A. Davies, M.R.J. Gibbs, D. Kendall, and R.V. Major: *J. Magn. Magn. Mater.*, 2000, vols. 215–216, pp. 272–75.
22. V.H. Duong, R. Sato Turtelli, and R. Grössinger: *IEEE Trans. Magn.*, 1996, vol. 32, pp. 4821–23.
23. B.J. Tate, B.S. Parmar, I. Todd, H.A. Davies, M.R.J. Gibbs, and R.V. Major: *J. Appl. Phys.*, 1998, vol. 83 (11), pp. 6335–37.